MATERIALS SCIENCE

Unconventional cross-step growth of monolayer MoS_2 on sapphire

Yangkun Zhang[1,2]†, Xudan Zhang[1,2]†, Xuhui Wang[1,2]†, Xiuzhen Li[1,2], Zhiheng Huang[1,2], Jingwei Dong[1,2], Zitian Pan[1,2], Jundong Zhu[1,2], Aomiao Zhi[1,2], Jiaojiao Zhao[1,2], Kunshan Ji[1,2], Fankun Wang[1,2], Wei Yang[1,2], Hua Yu[3], Xuedong Bai[1,2], Na Li[3], Dongxia Shi[1,2], Gang Wang[1,2], Shixuan Du[1,2], Jinbo Pan[1,2]*, Luojun Du[1,2]*, Guangyu Zhang[1,2]*

Regarding thin film growth, it has been widely recognized that the film typically follows the surface texture and high sharp steps potentially lead to growth termination and film discontinuity. Here, we demonstrate an abnormality that monolayer MoS_2 grown on *C*-plane sapphire is able to cross sharp steps up to ~10 nm in height. Assisted by theoretical simulations, we unveil that the cross-step growth of monolayer MoS_2 results from the competition between its deformation energy cost and adsorption energy gain. Notably, cross-step growth leads to the formation of one-dimensional (1D) ripples on target substrates after transfer, resulting in symmetry breaking and strain engineering to trigger anisotropic properties and boost transistor performances. The room-temperature mobility (on-state current) along the ripple direction is improved by ~67.6% (~118.4%) compared to that perpendicular to the ripple direction. Our work showcases an exotic cross-step growth paradigm to create and manipulate 2D materials, promising the prospect for a broad portfolio of emerging electronic, photonic, and optoelectronic applications.

INTRODUCTION

Two-dimensional (2D) materials with emergent properties that are unattainable in their bulk counterparts have emerged as highly promising for diverse technological advances in electronics, photonics, and optoelectronics (*1*–*5*). Reliable synthesis of high-quality 2D materials is a first and necessary step toward their real-world applications and stands as one of the most important directions in the current 2D realm (*6*–*11*). Notably, substrate steps are found to play a decisive role in governing the synthesis of 2D materials, especially the high-quality, single-crystalline 2D materials. To date, basically all noncentrosymmetric 2D single crystals, e.g., monolayer transition-metal dichalcogenides, are synthesized through step engineering (*12*–*24*).

Regarding this step-guided growth of 2D wafers, a natural question now arises: What is the height limit of steps that 2D materials can cross over, and could this capability transcend the conventional thin-film growth paradigm? Note that, in the conventional thin-film epitaxy, it has been widely recognized that the as-grown film typically follows the surface texture, and high sharp surface steps would lead to growth termination and film discontinuity due to the additional Ehrlich-Schwoebel barriers (*25*–*30*).

In this work, we demonstrate an unprecedented paradigm where the monolayer MoS_2 epitaxially grown on *C*-plane sapphire can cross over sharp steps up to ~10 nm in height (more than 15 times of the thickness of monolayer MoS_2). To the best of our knowledge, this represents the first experimental observation of this high-step tolerance in the epitaxial growth of 2D materials and also conventional thin films. Guided by first-principles calculations, we pinpoint the underlying origin of the cross-step growth of monolayer MoS_2 on sapphire to be the competition between deformation energy cost and adsorption energy gain. The cross-step growth paradigm facilitates the opportunities not only to create but also to manipulate 2D materials. By transferring the as-grown cross-step films to target substrates, the freestanding MoS_2 monolayers enabled by cross-step growth transforms into 1D ripples. This results in symmetry breaking and strain engineering to trigger the exotic anisotropic properties and boost the device performances. The room-temperature electron mobility (on-state current) along the ripple direction is improved by ~67.6% (~118.4%) compared to that perpendicular to the ripple direction.

RESULTS

Cross-step growth of monolayer MoS_2 on sapphire

To demonstrate the cross-step growth of monolayer MoS_2, *C*-plane (0001) sapphires with a large miscut angle of ~4° toward *M*-axis (defined as *C*/*M*-4°) are used. We highlight that introducing a larger miscut angle facilitates the reconstruction of higher steps by annealing under the experimentally accessible temperature owing to higher surface instability (*31*). Figure 1 (A and B) presents the atomic force microscopy (AFM) images of sapphire surfaces before (Fig. 1A) and after annealing (Fig. 1B) at ~1300°C for 4 hours in the presence of oxygen. Obviously, after thermal annealing, the sapphire surface is reconstructed into atomically flat terraces separated by dense sharp steps up to ~10.8 nm in height. It is noteworthy that the step height is controllable by adjusting the annealing temperature (fig. S1).

Figure 1C shows the optical microscopy image of a monolayer MoS_2 grown on the annealed sapphire substrate using custom-designed oxygen-assisted chemical vapor deposition (CVD) system (fig. S2) (*11*, *32*, *33*). It is noteworthy that the introduction of oxygen can strongly accelerates the reaction kinetics and result in a substantially higher growth rate, e.g., by 10 times, than conventional CVD approaches (*33*, *34*). The size of monolayer MoS_2 in the direction

[1]Beijing National Laboratory for Condensed Matter Physics, Institute of Physics, Chinese Academy of Sciences, 100190 Beijing, China. [2]School of Physical Sciences, University of Chinese Academy of Sciences, 100049 Beijing, China. [3]Songshan Lake Materials Laboratory, Dongguan, 523808 Guangdong, China.
*Corresponding author. Email: jbpan@iphy.ac.cn (J.P.); luojun.du@iphy.ac.cn (L.D.); gyzhang@iphy.ac.cn (G.Z.)
†These authors contributed equally to this work.

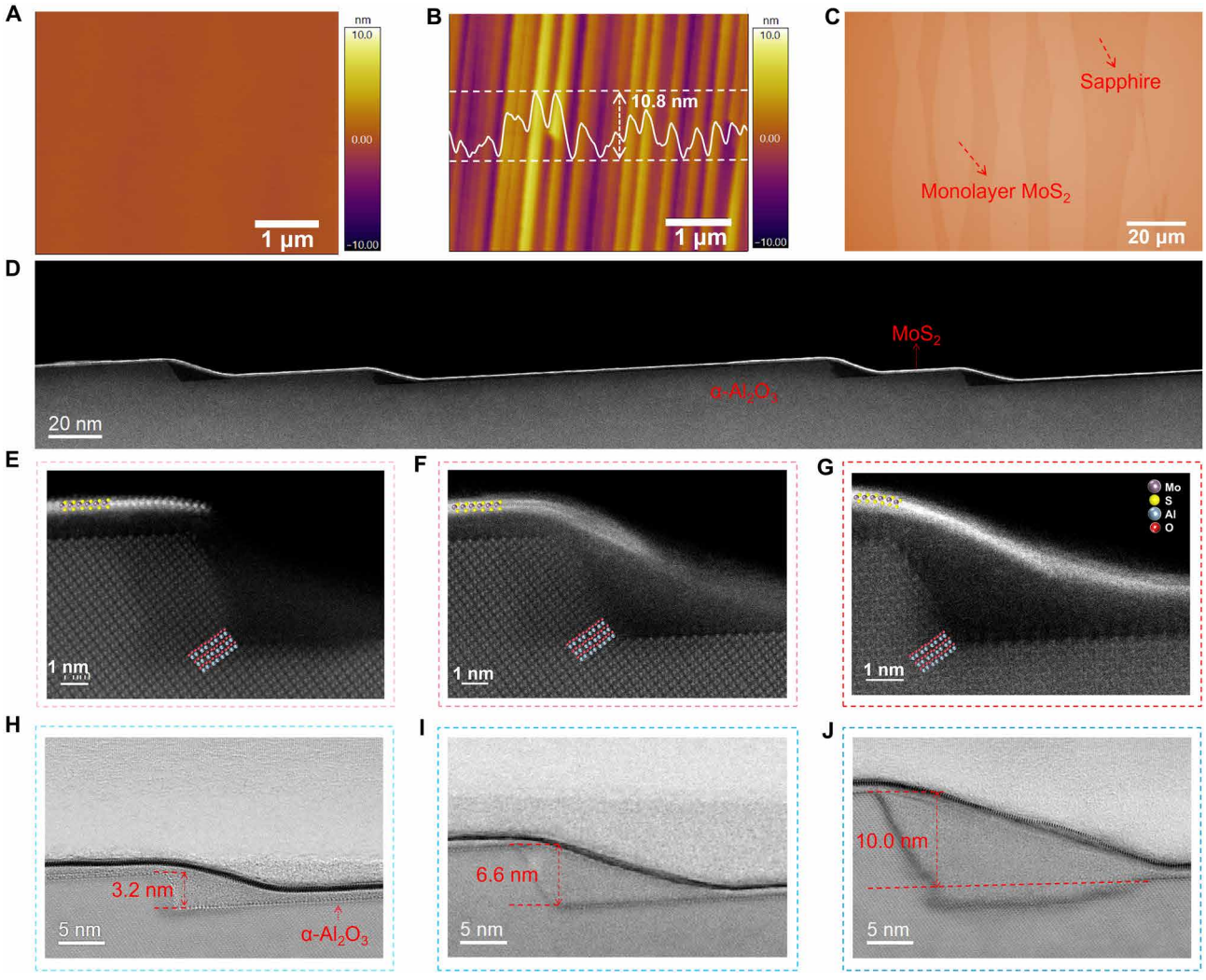

Fig. 1. Cross-step growth of monolayer MoS_2 on sapphire. (**A** and **B**) AFM images of the *C/M*-4° sapphire before (A) and after annealing at ~1300°C for 4 hours (B). A height profile is superimposed in (B), indicating steps up to ~10.8 nm in height. Scale bar, 1 μm. (**C**) Optical microscopy image of monolayer MoS_2 grown on sapphire shown in (B). Scale bar, 20 μm. (B) and (C) are reused images of fig. S1 (F and J, respectively). (**D**) Bright-field cross-sectional STEM image of monolayer MoS_2 grown on sapphire. Scale bar, 20 nm. (**E** to **G**) Close-up inspection of cross-sectional STEM images of monolayer MoS_2 at different step-crossing stages. Scale bars, 1 nm. (**H** to **J**) Dark-field cross-sectional STEM images of the cross-step growth of monolayer MoS_2 on sapphire with step heights of ~3.2 nm (H), ~6.6 nm (**I**) and ~10.0 nm (J). Scale bars, 5 nm. Panels (H), (I), and (J) are reused images of fig. S3 (B, E, and I, respectively).

perpendicular to the steps can reach up to ~20 μm, two orders of magnitude larger than the terrace width. This suggests that the as-grown monolayer MoS_2 can cross a plethora of steps whose height can be more than 15 times the thickness of monolayer MoS_2 (i.e., ~0.6 nm). At first glance, this is fairly unexpected, as it is generally believed that the lateral growth of monolayer MoS_2 would stop upon encountering a high surface step (*28*, *30*). To confirm that the monolayer MoS_2 can cross steps up to ~10 nm in height, we perform the cross-sectional scanning transmission electron microscopy (STEM) measurements (Fig. 1D). Instead of stopping growth near the steps, the as-grown monolayer MoS_2 can cross sharp steps in a freestanding manner. The exotic cross-step growth paradigm of monolayer MoS_2 on sapphires is further supported by a close-up inspection of the cross-sectional STEM at different stages when crossing the steps (Fig. 1, E to G) and also by series of different samples with step heights ranging from ~2.4 to ~10 nm (Fig. 1, H to J, and fig. S3).

Underlying mechanism of cross-step growth

The cross-step growth paradigm of monolayer MoS_2 on sapphire transcends the previous understanding. To figure out the underlying mechanism of cross-step growth of monolayer MoS_2, we carry out ab initio calculations within the context of the first-principles density functional theory (DFT). Figure 2A illustrates the as-grown monolayer MoS_2 on sapphire, directly following the surface steps. Obviously, the monolayer MoS_2 would undergo bending deformation to reside on the surface step, and the bending curvature of the monolayer MoS_2 ($1/R$) depends on the step angle θ. It is noteworthy that θ is defined as the angle between the surface terrace and step (Fig. 2A) and therefore reflects the steepness of the step. Because of the bending

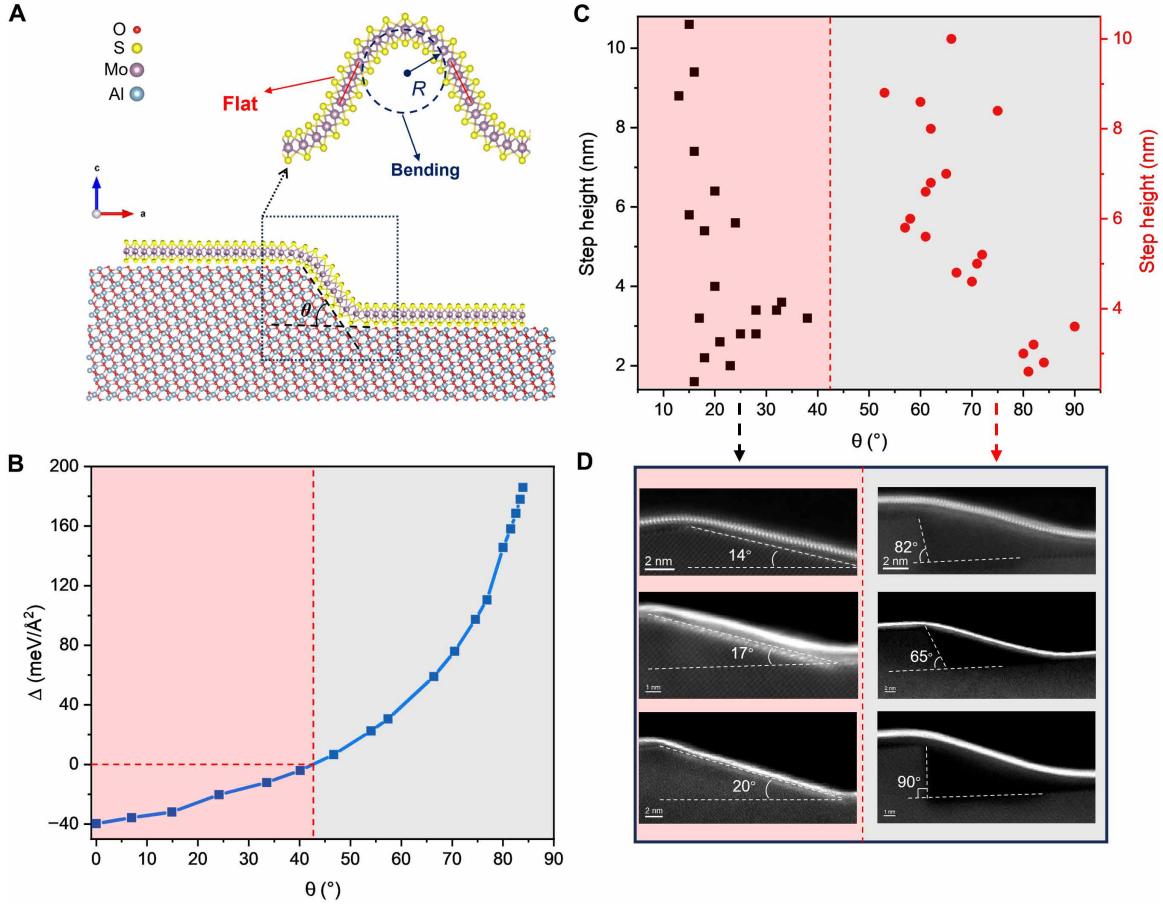

Fig. 2. Underlying mechanism of the cross-step growth of MoS_2. (**A**) Schematic diagram for the as-grown monolayer MoS_2 on sapphire, directly following the surface steps and undergoing deformation with bending curvature of 1/*R*. (**B**) Calculated Δ against θ. (**C**) Statistical results for more than 40 MoS_2 samples grown on sapphire with different step angle θ and step height. The red (black) data points correspond to the growth of monolayer MoS_2 in a cross-step manner (following the step). (**D**) Typical cross-sectional STEM images for the as-grown monolayer MoS_2 that follows the step (left three panels) and cross the step in a freestanding way (right three panels). Right and left panels of (D) are reused images of figs. S11 and S12, respectively.

deformation, there is a deformation energy cost E_{def} for monolayer MoS_2. E_{def} increases with the bending curvature and thus θ (fig. S8A), while it is essentially irrelevant to the crystal orientation of the bending, i.e., zigzag and armchair directions (fig. S8B). On the other hand, the interactions between monolayer MoS_2 and the sapphire step would result in an adsorption energy gain E_{ads} (fig. S9). The competition between $_{ads}$ and E_{ads}, defined as $\Delta = E_{def} - E_{ads}$, determines a specific growth mode. If $\Delta \leq 0$, then the growth of monolayer MoS_2 preferentially tends to follow the surface steps since the adsorption energy gain is larger than the deformation energy cost. By contrast, the monolayer MoS_2 would cross the sapphire steps in a cross-step manner when $\Delta > 0$ because the deformation energy cost dominates the growth process.

The calculated Δ as a function of θ is shown in Fig. 2B. Clearly, when the step angle θ exceeds a critical value $\theta_c = \sim 42°$, the adsorption energy gain is insufficient to overcome the deformation energy cost and Δ becomes greater than zero, suggesting the cross-step growth of monolayer MoS_2. It is noteworthy that the *M*-plane $(10\bar{1}0)$ of sapphire, which give rises to the largest adsorption energy gain (fig. S9), is adopted here as the step plane to calculate the Δ. When considering other high symmetry planes, such as O- and Al-terminated *C*-plane (0001), the calculated Δ against θ are nearly the same, except that there is some difference in the critical angle θ_c (fig. S8, C and D). It is worth noting that our model predicts a dependence on step angle θ regardless of step height. This arises because growth kinetics are not incorporated into our model. Regarding step height, its primary influence lies in governing the growth kinetics. In our experiments, the effect of step height on growth is observed. As shown in fig. S10, the growth rate ratio *r* along the step direction and perpendicular to the step direction increases with increasing step height, indicating that the growth perpendicular to the step direction is hindered.

Guided by the first-principles calculations, we thus perform the growth of monolayer MoS_2 on *C*-plane sapphires substrates with varying step angles and heights and then conduct the cross-sectional STEM measurements. Figure 2C shows the statistical results for more than 40 samples. Regardless of the step height, monolayer MoS_2 crosses the steps in a freestanding manner when $\theta > 45° \pm 5°$ (Fig. 2D and fig. S11), while the growth of monolayer MoS_2 follows the step when $\theta > 45° \pm 5°$ (Fig. 2D and fig. S12). The good agreement between theoretical calculations and experimental results explicitly unravels that the competition between deformation energy

cost and adsorption energy gain underlies the cross-step growth of monolayer MoS_2.

Symmetry-breaking engineering and anisotropic properties

The suspended MoS_2 near the step edges enabled by the cross-step growth, in principle, would transform into 1D ripples when transferred to a flat target substrate, such as the commonly used SiO_2/Si substrates (Fig. 3A). This offers extraordinary opportunities to engineer the rotational symmetry breaking and thus underpin intriguing anisotropic electronic and optoelectronic properties (*35*–*37*). Meanwhile, the presence of freestanding regions in the as-grown monolayer MoS_2 substantially reduces its coupling to the sapphire substrate. The relatively weak coupling is further confirmed by both Raman spectroscopy (fig. S13) and hexagonal boron nitride pick-up experiments (fig. S14), thereby facilitating the transfer to target substrates in a simple etching-free manner (*38*). Figure 3B shows the photograph of a monolayer MoS_2 film peeled off directly by a heat release tape without the aid of any chemical etchant (only deionized water is used) from the sapphire substrate with step height of ~10 nm. The inset of Fig. 3B shows the monolayer MoS_2 film transferred onto a SiO_2/Si substrate by removing the heat release tape. The zoom-in optical microscope images at nine random locations indicate that the transferred monolayer MoS_2 film is intact, clean, and uniform (fig. S15). It is noteworthy that, for conventional MoS_2 grown on sapphire with mono-/bi-atomic steps, transfer typically requires a chemical etchant (e.g., KOH solution) to etch the sapphire layer beneath the MoS_2 film (*38*–*40*).

Figure 3C presents a typical AFM height image of the square region in Fig. 3B. More AFM images can be found in fig. S16. Notably, a range of 1D ripples orientated along the step direction can be seen. These 1D ripples are ~200 nm in width and ~0.7 to 2.0 nm in height (inset of Fig. 3C). The 1D ripple structure breaks the rotational symmetry and thus reduces the point symmetry from D_{3h} to C_{2v}, giving rise to emergent anisotropic properties. To confirm the crystal symmetry breaking and anisotropic properties, we perform the polarization angle φ-resolved Raman measurements under the copolarized configuration (i.e., the polarizations of incident and emission light are parallel to each). φ is defined as the angle between the polarization of the excitation laser and the direction of 1D ripples. Figure 3D shows the normalized intensity ratio between E_{2g} and A_{1g} modes against the polarization angle φ for a 1D ripple MoS_2 film transferred from sapphires with step height of ~10 nm (orange dots) and a conventional ripple-free MoS_2 film transferred from sapphires with step height of ~0.2 nm (blue dots). For the conventional ripple-free MoS_2 sample, the intensity ratio between E_{2g} and A_{1g} modes basically does not change with φ, coinciding with the results of D_{3h} point group symmetry (note S1). In stark contrast, for 1D ripple MoS_2, the intensity ratio between E_{2g} and A_{1g} modes strongly depends on

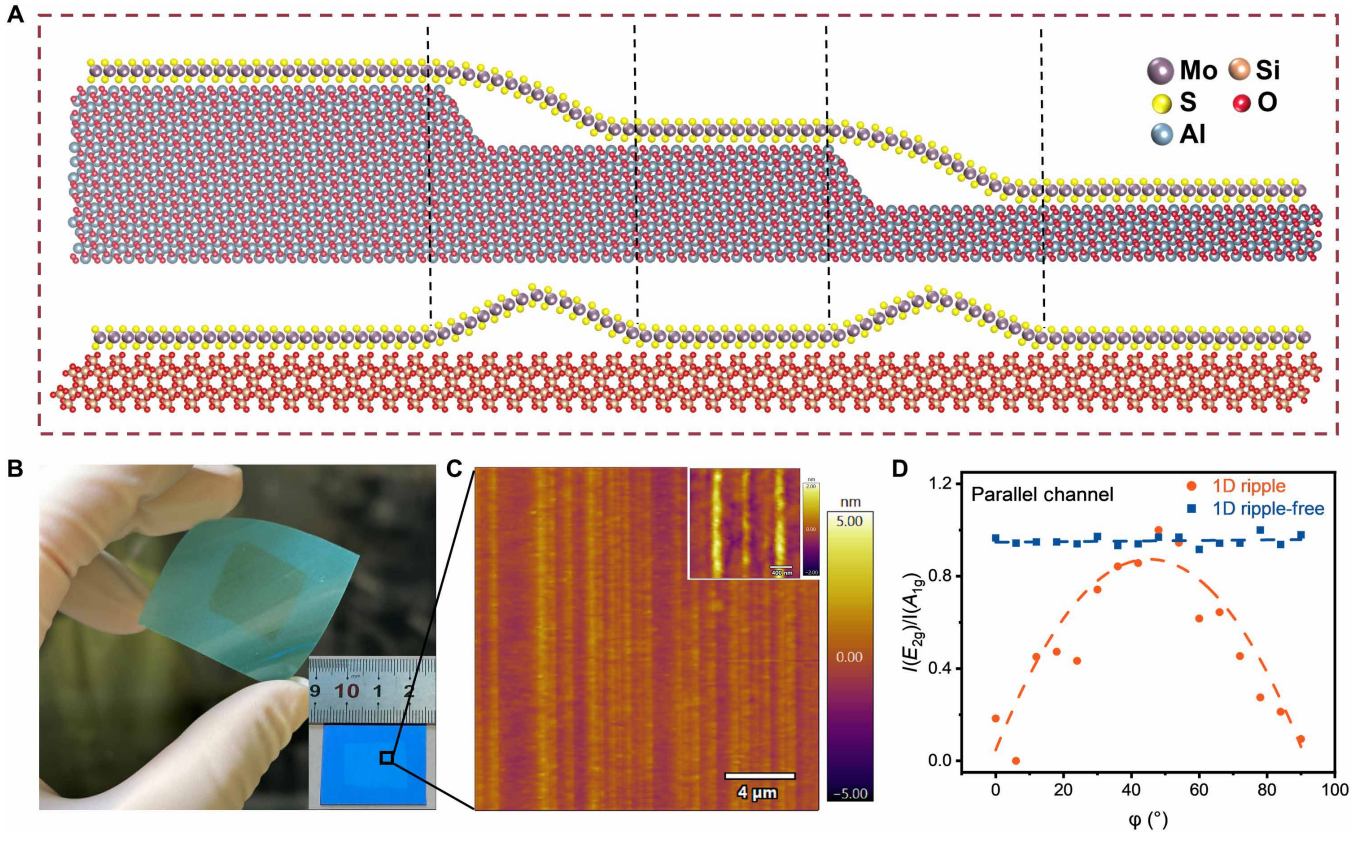

Fig. 3. Symmetry breaking engineering and anisotropic properties. (**A**) Top: Schematic diagram of the cross-step growth of monolayer MoS_2 on sapphire. Bottom: Schematic illustration of the 1D ripple formation when transferred to a flat target substrate. (**B**) Photograph of a monolayer MoS_2 film peeled off by heat release tape from sapphire with ~10 nm step heights. The lower right inset is a photo of the MoS_2 film transferred onto a SiO_2/Si substrate by removing the heat release tape. (**C**) AFM image taken from the square area indicated in (B). The upper right inset is a zoom-in image. (**D**) Normalized intensity ratio between E_{2g} and A_{1g} modes against φ for the MoS_2 films on Si/SiO_2 substrate transferred from sapphires with step heights of ~0.2 nm (blue dots) and ~10 nm (orange dots).

φ, evidencing the symmetry breaking and intriguing anisotropic properties (*36*, *37*). Moreover, the intensity ratio between E_{2g} and A_{1g} modes for 1D ripple MoS_2 can be well described by the equation derived from C_{2v} point group symmetry (orange line)

$$\frac{I(E_{2g})}{I(A_{1g})} = \frac{d^2\sin^2 2\varphi}{\left(a\cos^2\varphi + b\sin^2\varphi\right)^2} \quad (1)$$

where *a*, *b*, and *d* are matrix elements of the Raman tensor (note S1). The good consistency between the experimental observations and the results derived from C_{2v} point group elucidates explicitly the crystal symmetry breaking of the 1D MoS_2 ripples.

Boosted device performance

In addition to the symmetry breaking, the 1D ripple structure might also induce anisotropic strain field and improve the transistor performance according to previous studies (*41*–*45*). Raman measurements uncover a uniaxial tensile strain of ~0.15% (fig. S17). To verify this, we thus fabricate field effect transistors (FETs) based on the 1D ripple MoS_2 transferred from sapphires with step heights of ~10 nm. Figure 4 (A and B) illustrates the device geometry under vertical (parallel) configuration with Ti-Au-Ti as the back-gate electrode, 20-nm Al_2O_3 as the dielectric layer, and 1D ripple MoS_2 as the channel materials (see Materials and Methods for more details).

Figure 4C plots the output characteristic curves for a typical 1D ripple MoS_2 device with channel length/width of 2/4 μm under parallel configuration. The overall linear I_{ds}-V_{ds} output characteristics suggest an Ohmic contact behavior. Figure 4D presents the transfer characteristic curves for a typical 1D ripple MoS_2 device under both parallel (pink line) and vertical configurations (blue line). A ripple-free device with monolayer MoS_2 transferred from sapphires with step height of ~0.2 nm is also included as the control sample (green line). The 1D ripple MoS_2 devices display anisotropic electrical properties, and the on-state current under parallel configuration is much larger than that under vertical configuration and higher than that in the ripple-free device. It is noteworthy that for the conventional ripple-free monolayer MoS_2 devices, the electrical properties, such as on-state current and field-effect mobility, are isotropic (fig. S18), coinciding with the Raman results (Fig. 3D) and D_{3h} point group symmetry.

Figure 4E shows a statistical analysis of the on-state currents for 1D ripple MoS_2 devices under both parallel (bottom panel) and vertical configurations (top panel), as well as the ripple-free monolayer MoS_2 devices (middle panel). Notably, a substantial improvement in on-state currents can be seen for 1D ripple MoS_2 devices under parallel configuration. According to Lorentz distribution fittings, the average on-state current for 1D ripple MoS_2 devices under the parallel configuration is ~107 μA, which is boosted by ~118.4% compared to that under the vertical configuration (i.e., ~49 μA) and improved by

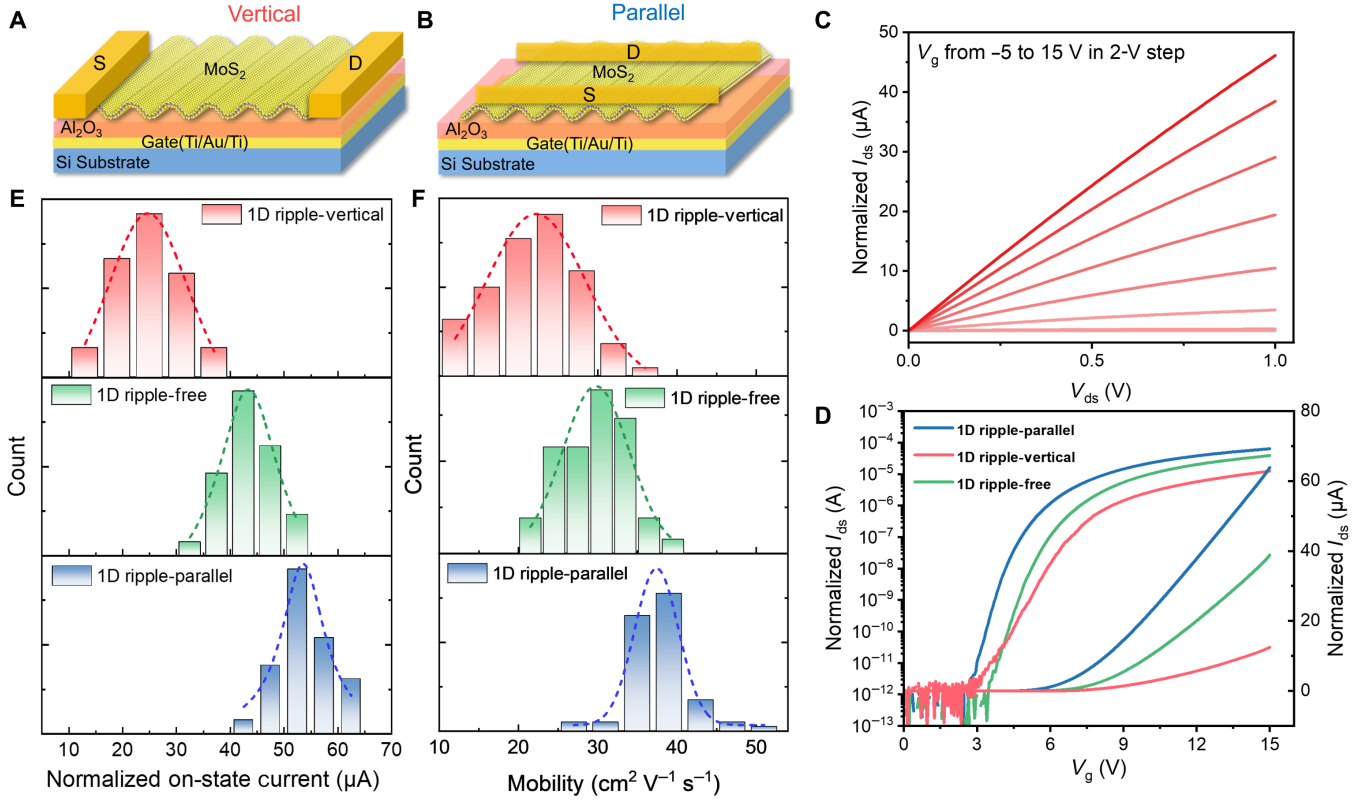

Fig. 4. Electrical characteristics and boosted transistor performance. (**A** and **B**) Schematic diagram of back-gate 1D ripple MoS_2 devices under vertical (A) and parallel configurations (B). (**C**) Output curves of the a typical 1D ripple MoS_2 device with channel length/width of 2/4 μm under parallel configuration. Back-gate voltages V_g is sweeping from −5 to 15 V with a step of 2 V. (**D**) Transfer curves of 1D ripple MoS_2 devices under parallel (blue) and vertical configurations (pink), as well as a conventional ripple-free device (green). (**E** and **F**) Statistical analysis of the normalized on-state currents (E) and mobility (F) for 1D ripple MoS_2 devices under parallel (bottom panel) and vertical configurations (top panel), as well as a conventional ripple-free monolayer MoS_2 device (middle panel).

~25.3% as well against the ripple-free devices (i.e., ~87 μA). Furthermore, the field-effect mobility μ is extracted by $\mu = G_m \frac{L}{WC_i V_{ds}}$, where G_m is the transconductance, C_i denotes the gate capacitance, V_{ds} is the source-drain bias, and L and W are channel length and width, respectively. To ensure consistency and eliminate hysteresis-induced systematic errors, all mobility values were calculated exclusively from reverse sweep transfer curves in the strong accumulation region, where all devices satisfy the linear region condition. Figure 4F shows a statistical analysis of μ at $V_{ds} = 1.0$ V for 1D ripple MoS_2 devices under both parallel (bottom panel) and vertical configurations (top panel), as well as ripple-free monolayer MoS_2 devices (middle panel). The average μ of 1D MoS_2 ripple devices under the parallel configuration is ~37.7 $cm^2 s^{-1} V^{-1}$, which is enhanced by ~67.6% compared to that under the vertical configuration (i.e., ~22.5 $cm^2 s^{-1} V^{-1}$) and also improved by ~26.1% against the ripple-free devices (i.e., ~29.9 $cm^2 s^{-1} V^{-1}$). The improvements in field-effect mobility and on-state current of 1D ripple MoS_2 devices under the parallel configuration are in good harmony with previous results (*41*–*45*) and are benefitted from the strain-trigged change of the band structure, which can lead to a reduction of electron and hole effective masses and electron-phonon scattering rates.

DISCUSSION

We demonstrate an unconventional cross-step growth paradigm wherein monolayer MoS_2 grown on sapphire can cross over steps up to ~10 nm in height (more than 15 times of the monolayer MoS_2 thickness). On the basis of first-principles calculations, we unveil that the cross-step growth of monolayer MoS_2 results from the competition between its deformation energy cost and adsorption energy gain. The suspended monolayer MoS_2 enabled by cross-step growth transforms into 1D ripples when transferred to target substrates, resulting in symmetry breaking and strain engineering to induce exotic anisotropic properties and boost the transistor performance. The room-temperature mobility (on-state current) along the ripple direction is improved by ~67.6% (~118.4%) compared to that perpendicular to the ripple direction. In addition, 1D ripple MoS_2 FETs are relatively stable, with negligible degradation in their electrical performance after 1 week (fig. S20). Our work showcases an exotic growth paradigm to create and manipulate 2D materials, promising the prospect for emerging technological applications in electronics, photonics, and optoelectronics.

MATERIALS AND METHODS

Growth of monolayer MoS_2 on sapphire

Single-sided polished *C*-plane (0001) sapphire substrates with a large miscut angle of ~4° toward the *M* axis were purchased from CRYSCORE OPTOELECTRONIC LIMITED. Then, the sapphire substrates were annealed to reconstitute the surface at a high temperature (e.g., ~900°, ~1100°, ~1200°, and ~1300°C) for 4 or 6 hours in the presence of oxygen. The growth of monolayer MoS_2 was achieved in a custom-designed three-temperature zone CVD system with multi-sources design. Typically, sulfur powder (Shanghai Aladdin Biochemical Technology, 99.999%, 25 g) was placed in the center mini-tube flowed with 40–standard cubic centimeter per minute (sccm) Ar, 85 cm from the sapphire substrate. MoO_3 powder (Alfa Aesar, 99.999%, 210 mg) was pressed into thin flacks by a hydraulic press and divided into three equal parts, which were individually placed in three quartz tubes with equilateral triangular distribution flowed with Ar/O_2 (40/2 sccm), 42 cm from the sapphire substrate, and the other three empty tubes are also flowed with Ar/O_2 (40/2 sccm). During the growth, the sulfur powder was heated to 180°C by a heating mantle in the temperature zone I. The MoO_3 flacks and sapphire substrate were heated to 580°C and 930°C in the temperature zones II and III, respectively. In addition, the pressure of CVD system was kept below 1 torr during the growth process. All zones ramped to target temperatures within 30 min, held for 20 min (continuous film), and then naturally cooled to room temperature under a constant Ar flow (160 sccm).

Structural and spectroscopic characterizations

The cross-sectional MoS_2/sapphire samples were fabricated in a Thermo Scientific Scios 2 system by focused ion beam (FIB) technology including coating with a protective layer at a polishing voltage of 5 kV (16-pA current). To minimize sample damage caused by ion beam milling during the FIB process, the MoS_2 sample surface was coated with a mechanically exfoliated *h*-BN (~60 nm), and then an Au film (~10 nm) was deposited by Gold Spray Meter. In addition, the residual contamination from the sample surface was removed in a precision ion polishing system at 2 kV (8.9-pA current). The FIB cut direction is always chosen to be vertical to the sapphire step direction. The as-prepared FIB samples (8 μm by 2 μm) were further processed by gallium ion polishing (Gatan 691, at 2 kV and 8.9 pA) to remove surface contamination and damaged layers. The annular dark-field and annular bright-field STEM characterizations were performed by an aberration-corrected STEM (JEM-ARM200F) at 200 kV. AFM imaging was carried out by Asylum Research Cypher S under tapping mode using the tip AC240TS-R3 (Oxford instruments). Raman and photoluminescence spectra were collected with a HORIBA spectrometer (LabRAM HR Evolution) in a confocal backscattering configuration (confocal pinhole of 100 μm) at room temperature. A solid-state laser at 532 nm is focused onto the samples along the *z* direction by a 100× objective with a spot size less than 1.5 μm. To uncover the fascinating anisotropy, we perform the polarization angle-resolved Raman measurements under the copolarized configuration. The excitation laser beam is passed through a linear polarizer and then a half-wave plate. The half-wave plate can tune the polarization angle in the *xy* plane. The backscattered light is passed through the same half-wave plate. Another linear polarizer is placed in front of the nitrogen-cooled charge-coupled device to selectively detect the components parallel to the polarization of excitation laser.

Theoretical modeling and simulations

All calculations were performed using density functional theory and the plane-wave projector-augmented wave method (*46*) as implemented in the Vienna Ab-initio Simulation Package (VASP) code (*47*). An energy cutoff of 400 eV and a vacuum length of 15 Å were used for all materials. The criteria of energy and force convergence were set to 1.0×10^{-6} eV and 0.01 eV $Å^{-1}$, respectively. Nonlocal exchange correlation functional rvv10 of Sabatini was adopted to describe the long-range van der Waals interaction (*48*). A Gamma-centered Brillouin zone sampling grids of $4 \times 4 \times 1$, $3 \times 1 \times 1$, and $1 \times 8 \times 1$ was applied for the adsorption of MoS_2 on α-Al_2O_3 of *C* plane, the adsorption of MoS_2 on α-Al_2O_3 of *M* plane, and all MoS_2 ribbons, respectively. For ribbon with limited size, periodic boundary conditions were used in all directions, and a 15-Å vacuum space was inserted in both the ribbon-width direction and the out-of-plane direction.

Along the ribbon axial direction, the smallest bulk unit period was used, all atomic coordinates of the flat ribbon were relaxed, and the structure of bent ribbon was obtained by fixing the distance between the two edges of a ribbon during structure relaxation. Specifically, this was achieved by fixing the outermost edge atoms (Mo atom). For periodically curved MoS_2 ribbon, all structures were fully relaxed in all directions.

Device fabrications and measurements

To fabricate back-gate FET, 15-nm Ti (3 nm)/Au (10 nm)/Ti (2 nm) is patterned and deposited on silicon substrate with 300-nm silicon oxide as local back gate. Next, 20-nm Al_2O_3 is applied as dielectric insulator using atomic layer deposition at a temperature of 200°C, using water and trimethyl aluminum as precursors. Subsequently, the MoS_2 film is transferred onto the Al_2O_3 layer from its initial growth substrate by a heat release tape assisted with deionized water (without the aid of any chemical etchant). The channel area is then defined using lithography, followed by reactive ion etching to shape it. Last, contact electrodes are defined by lithography and 43-nm Au (10 nm)/Ti (3 nm)/Au (30 nm) were finally deposited. The entire patterning procedure was carried out within the electron beam lithography system (Eline, Raith), using polymethyl methacrylate as the photoresist material. Metal electrodes are deposited using a custom-built electron beam deposition system and then subjected to the lift-off process. All electrical measurements in the main text are performed at room temperature with an Agilent semiconductor parameter analyzer under a base pressure of 10^{-6} torr.

Supplementary Materials

This PDF file includes:

Figs. S1 to S20
Notes S1 and S2
References

REFERENCES

1. Q. H. Wang, K. Kalantar-Zadeh, A. Kis, J. N. Coleman, M. S. Strano, Electronics and optoelectronics of two-dimensional transition metal dichalcogenides. *Nat. Nanotechnol.* **7**, 699–712 (2012).
2. Y. Liu, X. Duan, H. J. Shin, S. Park, Y. Huang, X. Duan, Promises and prospects of two-dimensional transistors. *Nature* **591**, 43–53 (2021).
3. K. S. Kim, J. Kwon, H. Ryu, C. Kim, H. Kim, E. K. Lee, D. Lee, S. Seo, N. M. Han, J. M. Suh, J. Kim, M. K. Song, S. Lee, M. Seol, J. Kim, The future of two-dimensional semiconductors beyond Moore's law. *Nat. Nanotechnol.* **19**, 895–906 (2024).
4. L. Du, M. R. Molas, Z. Huang, G. Zhang, F. Wang, Z. Sun, Moiré photonics and optoelectronics. *Science* **379**, eadg0014 (2023).
5. S. Manzeli, D. Ovchinnikov, D. Pasquier, O. V. Yazyev, A. Kis, 2D transition metal dichalcogenides. *Nat. Rev. Mater.* **2**, 17033 (2017).
6. G. Xue, B. Qin, C. Ma, P. Yin, C. Liu, K. Liu, Large-area epitaxial growth of transition metal dichalcogenides. *Chem. Rev.* **124**, 9785–9865 (2024).
7. T. Zhang, J. Wang, P. Wu, A. Y. Lu, J. Kong, Vapour-phase deposition of two-dimensional layered chalcogenides. *Nat. Rev. Mater.* **8**, 799–821 (2023).
8. J. Li, X. Yang, Z. Zhang, W. Yang, X. Duan, X. Duan, Towards the scalable synthesis of two-dimensional heterostructures and superlattices beyond exfoliation and restacking. *Nat. Mater.* **23**, 1326–1338 (2024).
9. Y. Wan, J. H. Fu, C. P. Chuu, V. Tung, Y. Shi, L. J. Li, Wafer-scale single-orientation 2D layers by atomic edge-guided epitaxial growth. *Chem. Soc. Rev.* **51**, 803–811 (2022).
10. C. Liu, T. Liu, Z. Zhang, Z. Sun, G. Zhang, E. Wang, K. Liu, Understanding epitaxial growth of two-dimensional materials and their homostructures. *Nat. Nanotechnol.* **19**, 907–918 (2024).
11. L. Li, Q. Wang, F. Wu, Q. Xu, J. Tian, Z. Huang, Q. Wang, X. Zhao, Q. Zhang, Q. Fan, X. Li, Y. Peng, Y. Zhang, K. Ji, A. Zhi, H. Sun, M. Zhu, J. Zhu, N. Lu, Y. Lu, S. Wang, X. Bai, Y. Xu, W. Yang, N. Li, D. Shi, L. Xian, K. Liu, L. Du, G. Zhang, Epitaxy of wafer-scale single-crystal MoS_2 monolayer via buffer layer control. *Nat. Commun.* **15**, 1825 (2024).
12. L. Wang, X. Xu, L. Zhang, R. Qiao, M. Wu, Z. Wang, S. Zhang, J. Liang, Z. Zhang, Z. Zhang, W. Chen, X. Xie, J. Zong, Y. Shan, Y. Guo, M. Willinger, H. Wu, Q. Li, W. Wang, P. Gao, S. Wu, Y. Zhang, Y. Jiang, D. Yu, E. Wang, X. Bai, Z. J. Wang, F. Ding, K. Liu, Epitaxial growth of a 100-square-centimetre single-crystal hexagonal boron nitride monolayer on copper. *Nature* **570**, 91–95 (2019).
13. T. A. Chen, C. P. Chuu, C. C. Tseng, C. K. Wen, H. S. P. Wong, S. Pan, R. Li, T. A. Chao, W. C. Chueh, Y. Zhang, Q. Fu, B. I. Yakobson, W. H. Chang, L. J. Li, Wafer-scale single-crystal hexagonal boron nitride monolayers on Cu (111). *Nature* **579**, 219–223 (2020).
14. K. Y. Ma, L. Zhang, S. Jin, Y. Wang, S. I. Yoon, H. Hwang, J. Oh, D. S. Jeong, M. Wang, S. Chatterjee, G. Kim, A. R. Jang, J. Yang, S. Ryu, H. Y. Jeong, R. S. Ruoff, M. Chhowalla, F. Ding, H. S. Shin, Epitaxial single-crystal hexagonal boron nitride multilayers on Ni (111). *Nature* **606**, 88–93 (2022).
15. P. Yang, S. Zhang, S. Pan, B. Tang, Y. Liang, X. Zhao, Z. Zhang, J. Shi, Y. Huan, Y. Shi, S. J. Pennycook, Z. Ren, G. Zhang, Q. Chen, X. Zou, Z. Liu, Y. Zhang, Epitaxial growth of centimeter-scale single-crystal MoS_2 monolayer on Au(111). *ACS Nano* **14**, 5036–5045 (2020).
16. S. H. Choi, H. J. Kim, B. Song, Y. I. Kim, G. Han, H. T. T. Nguyen, H. Ko, S. Boandoh, J. H. Choi, C. S. Oh, H. J. Cho, J. W. Jin, Y. S. Won, B. H. Lee, S. J. Yun, B. G. Shin, H. Y. Jeong, Y. M. Kim, Y. K. Han, Y. H. Lee, S. M. Kim, K. K. Kim, Epitaxial single-crystal growth of transition metal dichalcogenide monolayers via the atomic sawtooth Au surface. *Adv. Mater.* **33**, e2006601 (2021).
17. J. Wang, X. Xu, T. Cheng, L. Gu, R. Qiao, Z. Liang, D. Ding, H. Hong, P. Zheng, Z. Zhang, Z. Zhang, S. Zhang, G. Cui, C. Chang, C. Huang, J. Qi, J. Liang, C. Liu, Y. Zuo, G. Xue, X. Fang, J. Tian, M. Wu, Y. Guo, Z. Yao, Q. Jiao, L. Liu, P. Gao, Q. Li, R. Yang, G. Zhang, Z. Tang, D. Yu, E. Wang, J. Lu, Y. Zhao, S. Wu, F. Ding, K. Liu, Dual-coupling-guided epitaxial growth of wafer-scale single-crystal WS_2 monolayer on vicinal a-plane sapphire. *Nat. Nanotechnol.* **17**, 33–38 (2022).
18. T. Li, W. Guo, L. Ma, W. Li, Z. Yu, Z. Han, S. Gao, L. Liu, D. Fan, Z. Wang, Y. Yang, W. Lin, Z. Luo, X. Chen, N. Dai, X. Tu, D. Pan, Y. Yao, P. Wang, Y. Nie, J. Wang, Y. Shi, X. Wang, Epitaxial growth of wafer-scale molybdenum disulfide semiconductor single crystals on sapphire. *Nat. Nanotechnol.* **16**, 1201–1207 (2021).
19. H. Zhu, N. Nayir, T. H. Choudhury, A. Bansal, B. Huet, K. Zhang, A. A. Puretzky, S. Bachu, K. York, T. V. Mc Knight, N. Trainor, A. Oberoi, K. Wang, S. Das, R. A. Makin, S. M. Durbin, S. Huang, N. Alem, V. H. Crespi, A. C. T. van Duin, J. M. Redwing, Step engineering for nucleation and domain orientation control in WSe_2 epitaxy on c-plane sapphire. *Nat. Nanotechnol.* **18**, 1295–1302 (2023).
20. P. Yang, D. Wang, X. Zhao, W. Quan, Q. Jiang, X. Li, B. Tang, J. Hu, L. Zhu, S. Pan, Y. Shi, Y. Huan, F. Cui, S. Qiao, Q. Chen, Z. Liu, X. Zou, Y. Zhang, Epitaxial growth of inch-scale single-crystal transition metal dichalcogenides through the patching of unidirectionally orientated ribbons. *Nat. Commun.* **13**, 3238 (2022).
21. B. Qin, C. Ma, Q. Guo, X. Li, W. Wei, C. Ma, Q. Wang, F. Liu, M. Zhao, G. Xue, J. Qi, M. Wu, H. Hong, L. Du, Q. Zhao, P. Gao, X. Wang, E. Wang, G. Zhang, C. Liu, K. Liu, Interfacial epitaxy of multilayer rhombohedral transition-metal dichalcogenide single crystals. *Science* **385**, 99–104 (2024).
22. J. H. Fu, J. Min, C. K. Chang, C. C. Tseng, Q. Wang, H. Sugisaki, C. Li, Y. M. Chang, I. Alnami, W. R. Syong, C. Lin, F. Fang, L. Zhao, T. H. Lo, C. S. Lai, W. S. Chiu, Z. S. Jian, W. H. Chang, Y. J. Lu, K. Shih, L. J. Li, Y. Wan, Y. Shi, V. Tung, Oriented lateral growth of two-dimensional materials on c-plane sapphire. *Nat. Nanotechnol.* **18**, 1289–1294 (2023).
23. L. Wang, J. Qi, W. Wei, M. Wu, Z. Zhang, X. Li, H. Sun, Q. Guo, M. Cao, Q. Wang, C. Zhao, Y. Sheng, Z. Liu, C. Liu, M. Wu, Z. Xu, W. Wang, H. Hong, P. Gao, M. Wu, Z. J. Wang, X. Xu, E. Wang, F. Ding, X. Zheng, K. Liu, X. Bai, Bevel-edge epitaxy of ferroelectric rhombohedral boron nitride single crystal. *Nature* **629**, 74–79 (2024).
24. B. Wang, E. Wang, Y. Sheng, S. Zhang, A. Zhi, Y. Wang, J. Dong, Z. Pan, Z. Jia, C. Cui, J. Zhu, Y. Shen, W. Yang, D. Shi, S. Meng, K. Liu, L. Wang, H. Hong, Y. Wang, Z. Sun, G. Zhang, L. Du, Synthesis of rhombohedral WS_2/MoS_2 nanoribbons with enhanced nonlinear responses. *Chin. Phys. Lett.* **43**, 040802 (2026).
25. J. Venables, *Introduction to Surface and Thin Film Processes* (Cambridge Univ. Press, 2010).
26. G. Hlawacek, P. Puschnig, P. Frank, A. Winkler, C. Ambrosch-Drax, C. Teichert, Characterization of step-edge barriers in organic thin-film growth. *Science* **321**, 108–111 (2008).
27. C. Meng, J. Gao, R. Li, Y. Ning, Y. Chang, R. Mu, Q. Fu, X. Bao, Step-confined thin film growth via near-surface atom migration. *Nano Res.* **13**, 1552–1557 (2020).
28. J. Lu, M. Zheng, J. Liu, Y. Zhang, X. Zhang, W. Cai, Impact of sapphire step height on the growth of monolayer molybdenum disulfide. *Nanomaterials* **13**, 3056 (2023).
29. J. Lu, P. S. E. Yeo, Y. Zheng, H. Xu, C. K. Gan, M. B. Sullivan, A. H. Castro Neto, K. P. Loh, Step flow versus mosaic film growth in hexagonal boron nitride. *J. Am. Chem. Soc.* **135**, 2368–2373 (2013).
30. D. Ding, S. Wang, Y. Xia, P. Li, D. He, J. Zhang, S. Zhao, G. Yu, Y. Zheng, Y. Cheng, M. Xie, F. Ding, C. Jin, Atomistic insight into the epitaxial growth mechanism of single-crystal two-dimensional transition-metal dichalcogenides on Au(111) substrate. *ACS Nano* **16**, 17356–17364 (2022).

31. M. Yoshimoto, T. Maeda, T. Ohnishi, H. Koinuma, O. Ishiyama, M. Shinohara, M. Kubo, R. Miura, A. Miyamoto, Atomic-scale formation of ultrasmooth surfaces on sapphire substrates for high-quality thin-film fabrication. *Appl. Phys. Lett.* **67**, 2615–2617 (1995).
32. H. Yu, M. Liao, W. Zhao, G. Liu, X. J. Zhou, Z. Wei, X. Xu, K. Liu, Z. Hu, K. Deng, S. Zhou, J. A. Shi, L. Gu, C. Shen, T. Zhang, L. Du, L. Xie, J. Zhu, W. Chen, R. Yang, D. Shi, G. Zhang, Wafer-scale growth and transfer of highly-oriented monolayer MoS_2 continuous films. *ACS Nano* **11**, 12001–12007 (2017).
33. Q. Wang, J. Tang, X. Li, J. Tian, J. Liang, N. Li, D. Ji, L. Xian, Y. Guo, L. Li, Q. Zhang, Y. Chu, Z. Wei, Y. Zhao, L. Du, H. Yu, X. Bai, L. Gu, K. Liu, W. Yang, R. Yang, D. Shi, G. Zhang, Layer-by-layer epitaxy of multi-layer MoS_2 wafers. *Natl. Sci. Rev.* **9**, nwac077 (2022).
34. W. Chen, J. Zhao, J. Zhang, L. Gu, Z. Yang, X. Li, H. Yu, X. Zhu, R. Yang, D. Shi, X. Lin, J. Guo, X. Bai, G. Zhang, Oxygen-assisted chemical vapor deposition growth of large single-crystal and high-quality monolayer MoS_2. *J. Am. Chem. Soc.* **137**, 15632–15635 (2015).
35. L. Du, T. Hasan, A. Castellanos-Gomez, G. Bin Liu, Y. Yao, C. N. Lau, Z. Sun, Engineering symmetry breaking in 2D layered materials. *Nat. Rev. Phys.* **3**, 193–206 (2021).
36. L. Du, Y. Zhao, L. Wu, X. Hu, L. Yao, Y. Wang, X. Bai, Y. Dai, J. Qiao, M. G. Uddin, X. Li, J. Lahtinen, X. Bai, G. Zhang, W. Ji, Z. Sun, Giant anisotropic photonics in the 1D van der Waals semiconductor fibrous red phosphorus. *Nat. Commun.* **12**, 4822 (2021).
37. L. Li, W. Han, L. Pi, P. Niu, J. Han, C. Wang, B. Su, H. Li, J. Xiong, Y. Bando, T. Zhai, Emerging in-plane anisotropic two-dimensional materials. *InfoMat* **1**, 54–73 (2019).
38. T. F. Schranghamer, M. Sharma, R. Singh, S. Das, Review and comparison of layer transfer methods for two-dimensional materials for emerging applications. *Chem. Soc. Rev.* **50**, 11032–11054 (2021).
39. N. Li, Q. Wang, C. Shen, Z. Wei, H. Yu, J. Zhao, X. Lu, G. Wang, C. He, L. Xie, J. Zhu, L. Du, R. Yang, D. Shi, G. Zhang, Large-scale flexible and transparent electronics based on monolayer molybdenum disulfide field-effect transistors. *Nat. Electron.* **3**, 711–717 (2020).
40. Z. Wei, Y. Cai, J. Liu, L. Zhang, J. Zhao, J. Tang, L. Li, Q. Wang, H. Zhang, Z. Zhang, D. Shi, L. Du, Efficient, non-destructive transfer of wafer-scale monolayer MoS_2 by interface engineering. *Adv. Funct. Mater.* **36**, e17643 (2025).
41. H. K. Ng, D. Xiang, A. Suwardi, G. Hu, K. Yang, Y. Zhao, T. Liu, Z. Cao, H. Liu, S. Li, J. Cao, Q. Zhu, Z. Dong, C. K. I. Tan, D. Chi, C. W. Qiu, K. Hippalgaonkar, G. Eda, M. Yang, J. Wu, Improving carrier mobility in two-dimensional semiconductors with rippled materials. *Nat. Electron.* **5**, 489–496 (2022).
42. T. Liu, S. Liu, K. H. Tu, H. Schmidt, L. Chu, D. Xiang, J. Martin, G. Eda, C. A. Ross, S. Garaj, Crested two-dimensional transistors. *Nat. Nanotechnol.* **14**, 223–226 (2019).
43. M. Jaikissoon, Ç. Köroğlu, J. A. Yang, K. Neilson, K. C. Saraswat, E. Pop, CMOS-compatible strain engineering for monolayer semiconductor transistors. *Nat. Electron.* **7**, 885–891 (2024).
44. I. M. Datye, A. Daus, R. W. Grady, K. Brenner, S. Vaziri, E. Pop, Strain-enhanced mobility of monolayer MoS_2. *Nano Lett.* **22**, 8052–8059 (2022).
45. X. Liu, B. Erbas, A. Conde-Rubio, N. Rivano, Z. Wang, J. Jiang, S. Bienz, N. Kumar, T. Sohier, M. Penedo, M. Banerjee, G. Fantner, R. Zenobi, N. Marzari, A. Kis, G. Boero, J. Brugger, Deterministic grayscale nanotopography to engineer mobilities in strained MoS_2 FETs. *Nat. Commun.* **15**, 6934 (2024).
46. G. Kresse, D. Joubert, From ultrasoft pseudopotentials to the projector augmented-wave method. *Phys. Rev. B* **59**, 1758–1775 (1999).
47. G. Kresse, J. Furthmüller, Efficiency of ab-initio total energy calculations for metals and semiconductors using a plane-wave basis set. *Comput. Mater. Sci.* **6**, 15–50 (1996).
48. R. Sabatini, T. Gorni, S. De Gironcoli, Nonlocal van der Waals density functional made simple and efficient. *Phys. Rev. B* **87**, 041108 (2013).
49. X. Zhang, X. F. Qiao, W. Shi, J. Bin Wu, D. S. Jiang, P. H. Tan, Phonon and Raman scattering of two-dimensional transition metal dichalcogenides from monolayer, multilayer to bulk material. *Chem. Soc. Rev.* **44**, 2757–2785 (2015).
50. M. Liao, Z. Wei, L. Du, Q. Wang, J. Tang, H. Yu, F. Wu, J. Zhao, X. Xu, B. Han, K. Liu, P. Gao, T. Polcar, Z. Sun, D. Shi, R. Yang, G. Zhang, Precise control of the interlayer twist angle in large scale MoS_2 homostructures. *Nat. Commun.* **11**, 2153 (2020).
51. K. He, C. Poole, K. F. Mak, J. Shan, Experimental demonstration of continuous electronic structure tuning via strain in atomically thin MoS_2. *Nano Lett.* **13**, 2931–2936 (2013).
52. R. Loudon, The Raman effect in crystals. *Adv. Phys.* **50**, 813–864 (2001).
53. L. Du, J. Tang, Y. Zhao, X. Li, R. Yang, X. Hu, X. Bai, X. Wang, K. Watanabe, T. Taniguchi, D. Shi, G. Yu, X. Bai, T. Hasan, G. Zhang, Z. Sun, Lattice dynamics, phonon chirality, and spin–phonon coupling in 2D itinerant ferromagnet Fe_3GeTe_2. *Adv. Funct. Mater.* **29**, 1904734 (2019).

Acknowledgments

Funding: This work is supported by the National Key Research and Development Program of China (grant no. 2021YFA1202900) and the National Natural Science Foundation of China (NSFC, grant nos. 12422402, 62488201, 12274447, and 62204166). L.D. acknowledges the National Key R&D Program of China (grant no. 2023YFA1407000). D.S. acknowledges the National Key R&D Program of China (grant no. 2021YFA1400502). **Author contributions:** G.Z. and L.D. conceived and supervised the project. Y.Z. performed CVD growth and STEM characterizations. X.Z., J.P. and S.D. performed modeling and theoretical calculations. X.W. and G.W. performed the substrate annealing. X.L. and Y.Z. contributed to transistor fabrication, measurements and data analysis. Z.H., J.D., Z.P., Ju.Z., and F.W. carried out optical and dry pick-up experiments. A.Z., Ji.Z. and X.B. performed FIB characterizations and data analysis. K.J performed Raman characterizations. W.Y., H.Y., N.L., and D.S. contributed to the discussions. Y.Z., L.D. and G.Z. cowrote the manuscript, with input from all authors. **Competing interests:** The authors declare that they have no competing interests. **Data, code, and materials availability:** All data and code needed to evaluate and reproduce the results in the paper are present in the paper and/or the Supplementary Materials. This study did not generate new materials.

Submitted 9 December 2025
Accepted 25 June 2026
Published 31 July 2026
10.1126/sciadv.aee6153

ScienceAdvances

Unconventional cross-step growth of monolayer MoS_2 on sapphire

Yangkun Zhang, Xudan Zhang, Xuhui Wang, Xiuzhen Li, Zhiheng Huang, Jingwei Dong, Zitian Pan, Jundong Zhu, Aomiao Zhi, Jiaojiao Zhao, Kunshan Ji, Fankun Wang, Wei Yang, Hua Yu, Xuedong Bai, Na Li, Dongxia Shi, Gang Wang, Shixuan Du, Jinbo Pan, Luojun Du, and Guangyu Zhang

Sci. Adv. **12** (31), eaee6153. DOI: 10.1126/sciadv.aee6153